

Experimental Investigation of Stepped Fuel Grain Geometries in Hybrid Rocket Engines

C. Glaser^{*†}, R. Gelain^{**}, A. E. M. Bertoldi^{**}, J. Hijlkema^{*}, P. Hendrick^{**} and J. Anthoine^{*}

^{*}ONERA/DMPE, Université de Toulouse
F-31410 Mauzac, France

^{**}Aero-Thermo-Mechanics Department, Université Libre de Bruxelles
50 Avenue F. D. Roosevelt, 1050 Brussels, Belgium

christopher.glaser@onera.fr · riccardo.gelain@ulb.be · artur.elias.de.morais.bertoldi@ulb.be
patrick.hendrick@ulb.be · jouke.hijlkema@onera.fr · jerome.anthoine@onera.fr

[†]Corresponding author

Abstract

In this work, the effect of Forward Facing Steps (FFS) and Backward Facing Steps (BFS) on the Hybrid Rocket Engine's regression rate is investigated through test firings on both a classic cylindrical motor and a two-dimensional slab burner with optical access. It serves as a first experimental investigation into the proposal to distribute a set of steps along any predefined fuel port profile. For the cylindrical motor, a single FFS or BFS increased the total average regression rate by up to 48 % and 53 % respectively. On the slab burner, the local zones of high regression rate could be directly derived from the optical access during the burn and they correlate precisely to the regression rate profiles of the cylindrical cases.

Nomenclature

D_0	Initial Diameter	h_{res}	Spatial resolution
D_f	Final diameter	\dot{m}_{ox}	Oxidizer mass flow
D_{com}	Diameter of communicating vessel	m_f	Burnt fuel mass
D_{grain}	Grain mean diameter	t_b	Burn time
D	Outer diameter	t_{ign}	Ignition time
G_{avg}	Averaged mass flux	x_0	Lower axial boundary
I	Intensity	x_1	Upper axial boundary
V_{inj}	Injected volume	y_{max}	Maximum frame height
α	Angular displacement	z	Parallel displacement
d	Inner diameter		

1. Introduction

Hybrid Rocket Engines (HREs) are a promising technology to achieve a cheaper, more sustainable and competitive access to space. So far, liquid rocket engines and solid rocket motors have been preferred over HREs for launcher applications. This is due to the low maturity of HREs, as well as challenges related to low regression rate, combustion inefficiency, oxidizer-to-fuel ratio (O/F) shift during operation and high residual inert mass. Nonetheless, in recent

years, the new space launcher market calls also for cheap micro- and nano-launchers. HREs could help to fill this niche given their advantages (e.g. high performance, intrinsic safety, throttle-ability, flexibility and low cost), provided that some of the disadvantages are being solved. Starting in 2010, the number of publications on HREs increased considerably [1], proving the rising interest in the potential capabilities of HREs.

In previous work [2], we proposed to distribute a set of BFS and FFS (in the form of cylindrical fuel grains with varying inner diameter) along any predefined optimized profile as depicted in Figure 1. This way, three major advantages are anticipated:

1. Instead of 3D-printing complex fuel geometries, the fuel port profiles can now be approximated by a finite number of fuel cylinders with varying inner diameter.
2. The fuel port still exhibits the benefits its fuel port profile was optimized for, e.g. lower O/F shift during operation.
3. The set of steps increase turbulence, mixing, heat transfer and, thus, enhance the overall regression rate.

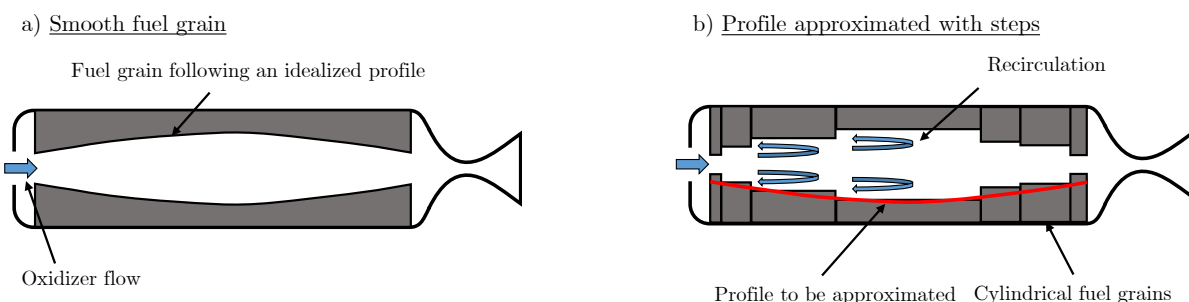


Figure 1: Approximation of fuel port profiles as proposed in [2]

In order to gain further insight into the phenomenon of regression rate enhancement through BFS and FFS, an experimental campaign is carried out on a lab-scale HRE using nitrous oxide (N_2O) and High-Density Polyethylene (HDPE) as propellants. Additionally, to investigate the effect of the steps on the regression rate also during the test, BFS and FFS geometries are further tested in a paraffin slab burner with optical access. The focus of the test campaign can be summarized as follows: The cylindrical motor will be equipped with fuel grains that consist of either a FFS or a BFS of 10 mm height in the middle. After each test, the fuel grains are investigated and their local regression rate profile as well as the space and time averaged regression rates assessed. Moreover, the tests will be compared to no-stepped reference cases to quantify the regression rate enhancement. This campaign is presented in Section 3. Additionally, with the use of the optical access of a 2D slab burner, the effect of the steps on the HRE flow-field and regression rate is investigated visually during the test and the results obtained will be correlated to the cylindrical motor campaign. The 2D step campaign will be explained in Section 4.

2. Turbulence Enhancing Devices in the Literature

The application of diaphragms, resembling both a FFS and BFS at the same time, and other turbulence and heat exchange enhancing devices in the solid fuel grain have proven to increase both regression rate and combustion efficiency due to the formation of recirculation zones. These zones increase turbulence, mixing as well as heat transfer and, as a consequence, lead to improved performance of the HREs. Here, we will concentrate on the effect of exemplary diaphragm and step research found in open literature. For an extensive collection of regression rate enhancing techniques through turbulence (among others) the reader is referred to [3]. In 1972, Gany and Timnat [4] increased the regression rate of a polyester HRE around 50 % by using a diaphragm in the middle of the fuel grain. Grosse [5] researched extensively the usage of diaphragms with different cross-section shapes in paraffin based motors and observed regression rate increments of 84 % downstream the 4-holed diaphragm. Dinesh and Kumar [6] exploited experimentally the fact that the regression rate enhancing effect of diaphragms relates directly to the recirculation zone length. For this reason, they distributed multiple diaphragms inside the fuel port to maintain the enhancing effect of the diaphragms throughout the fuel grain length. They found an ideal spacing for their motor of 2.7 times the recirculation zone length.

As for steps, Lee *et al.* [7] used a single BFS inside the fuel grain, thereby decreasing combustion instabilities and increasing the regression rate 50 % downstream the BFS. Sakashi *et al.* [8] tested a concave-convex design (effectively resembling a sequence of BFS and FFS) and observed 70-100 % increased regression rates. Later, Kumar and Joshi [9]

also created a grain of alternating steps using cylinders with two different inner diameters and increased the average regression rate between 30 and 55 %. To use a set of steps with different heights and widths to follow a predefined profile or any other geometry has neither been proposed or tested to the knowledge of the authors.

3. Axissymmetric *Stepperino* Campaign

To better understand the effect of steps inside fuel grains, different step configurations are evaluated experimentally in this section. In total, 9 tests have been carried out on the ULBHRM motor at ULB-ATM, and the impact on the regression rate has been assessed. These data, together with qualitative numerical results gathered in [2] will allow to develop a fully stepped design following a predefined profile as proposed in Figure 1 in future work.

3.1 Test Facilities

The test campaign has been carried out on the ULB-ATM Hybrid Rocket Engine [10], which has been designed to provide 1 kN of thrust for a burning time of 10 s, using liquid nitrous oxide as oxidizer and paraffin wax as a fuel. The nitrous oxide is pressurized at 60 bar with nitrogen and the average chamber pressure during the test campaign yielded around 16 bar. For our studies, we decided to use HDPE as fuel instead of paraffin, because the fuel consumption of paraffin could be too fast to assess the step in the fuel grains after the tests. It is to be noted that changing the fuel to HDPE is anticipated to have a rather dominant effect on the O/F values. This is due to the fact that the motor was initially optimized for paraffin fuels. Therefore, the fuel grain is rather short (118 mm), as paraffin has approximately 3-4 times the regression rate of HDPE. The short grain length together with the lower regression rates of polymer fuels will lead to an untypically high O/F. Nonetheless, since the high O/F will not have a qualitative impact on the regression rate profiles, we opted for HDPE.

Pressure measurements can be acquired in the engine and in the feed system. For the analysis of combustion instabilities, a piezoelectric pressure transducer can be used in the post-chamber as well. K-type thermocouples allow to measure the temperature of the oxidizer in the lines, and two load cells are used to measure the thrust of the engine and the variation of oxidizer mass in the tank. To estimate the N₂O mass flow, the weight loss of the N₂O tank is related to the burn time of the motor. For the injection, a showerhead injector is used, which yielded N₂O mass flow rates between 0.39 and 0.51 kg/s in our case. The engine parameters and the design process are described in more detail in reference [10].

3.2 Methods to Estimate Regression Rate Profiles

In the literature, several methods to estimate the regression rate after the burn are used. For this work, a longitudinal slicing method is applied to assess the local regression rate profiles. Moreover, for future work and to introduce a non-intrusive approach, we propose a new procedure labeled the *communicating vessel* method. In the following sections, both strategies are explained and their susceptibility to measurement errors assessed.

3.2.1 Longitudinal Slicing Method

This method is rather straight-forward. After the experimental campaign, the fuel grains are cut along their longitudinal axis. Next, the halves are digitized with a standard office scanner. With image processing tools such as *Fiji* [11], the local final inner diameter $D_f(x)$ of the fuel grain can be measured. Knowing the initial diameter, the temporally averaged local regression rate can be easily derived using the expression:

$$\dot{r}(x) = \frac{D_f(x) - D_0(x)}{2t_b} . \quad (1)$$

Moreover, the space and time averaged regression rate (over any interval of interest) can be calculated using:

$$\bar{r} = \frac{1}{x_1 - x_0} \int_{x_0}^{x_1} \dot{r}(x) dx . \quad (2)$$

While this method is rather easy to apply, special care has to be taken concerning the accuracy of the cut. There are two potential sources of errors in the slicing approach. The first is the parallel displacement of the cut from the axis. Figure 2 illustrates the relative error in the measurement of the diameter (measured diameter vs. real diameter) when the line of attack of the cut is displaced parallel to the grain axis. It becomes obvious that the relative error for large port fuel grains is well below an arbitrary threshold of 5 % relative error. For smaller fuel ports, the error becomes

more pronounced. However, the discrepancy stays below 5 % for displacements of 4 mm or less, which gives sufficient margin to apply the method. The grains presented in this study have been processed with a maximum displacement of 3 mm in one case, which for our grain diameters above 50 mm translates to an error of around 1 %.

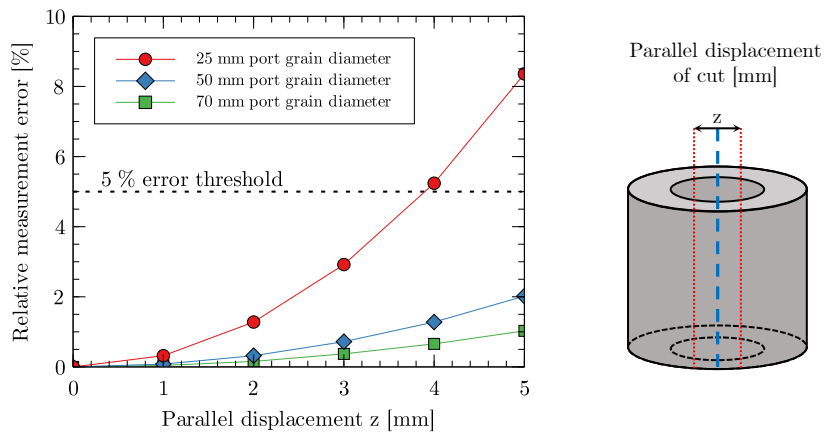


Figure 2: Parallel displacement error

Similar considerations of accuracy can be applied to the angular displacement of the saw. Figure 3 displays possible error values for different fuel port diameters and fuel grain lengths. Even for the small fuel grain port diameters of the 118 mm grain length (typical length of the ULB motor), all angular displacements of 4 degree and less have almost negligible relative measurement errors. For longer fuel grains (such as the ones used with the HyCAT motor at ONERA), the error gets more pronounced, especially for the small fuel ports. However, during the test campaign in this study (118 mm fuel grain), the angular displacement even with standard equipment was well below 2 degrees. It is to be stressed that angular displacements change the fuel port shape after the cut, as the measured diameters at the ends of the axis are smaller than the one in the middle. For small port grains with higher length, this effect needs to be considered.

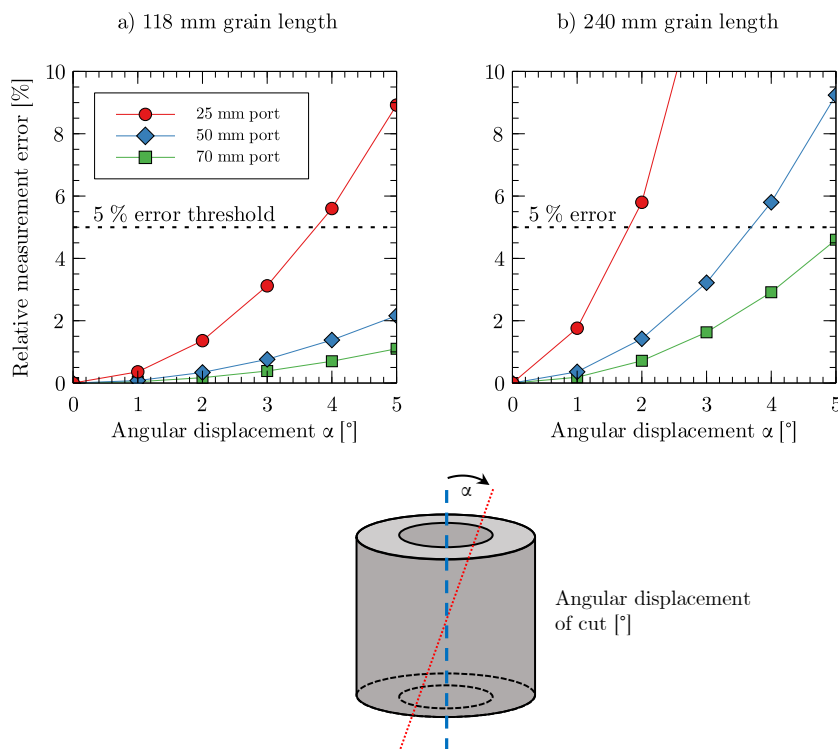


Figure 3: Angular displacement error

3.2.2 Communicating Vessel Method

One major downside of the slicing method is that the grains will be destroyed in the process. In the case of large errors in alignment, the test results can be possibly lost. This is why, as an additional non-destructive approach, we propose a method based on the principle of *communicating vessels* (see Figure 4). The fuel grain is connected with a hose to a

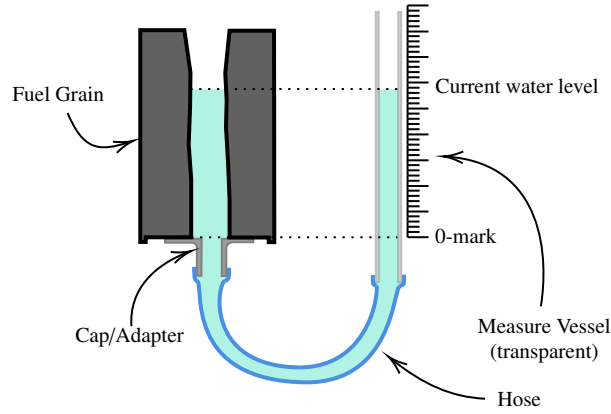


Figure 4: Scheme of the communicating vessel method

transparent tube. The idea is to fill the fuel port with water until the water level in the clear tube rises by a predefined distance, e.g. 10 mm. This distance represents the resolution (h_{res}) of the method. Knowing the volume of the injected water and the diameter in the transparent tube, the mean diameter inside the fuel grain can be reconstructed. Equation 3 describes how the profile of the diameter along the grain can be calculated based on the injected volume and desired axial resolution:

$$V_{inj}(n) = \pi \frac{D_{grain}^2(n) + D_{com}^2}{4} h_{res} \quad \Rightarrow \quad D_{grain}(n) = \sqrt{\frac{4V_{inj}(n)}{\pi h_{res}} - D_{com}^2}, \quad (3)$$

with $V_{inj}(n)$ being the injected volume at the n^{th} step, and $D_{grain}(n)$ the grain's mean diameter along the n^{th} step. D_{com} is the diameter of the (communicating) transparent vessel (assumed cylindrical). To assess the feasibility of this method, four tests have been conducted on grains with a known constant diameter (25 and 40 mm) and a 10 mm axial resolution, which yielded promising results. The overall mean relative errors at each axial position were around 1%, with some peaks near the beginning and end of the fuel grain. The errors were lower in the case of wider port-holes and the results were easily repeatable.

3.3 Intention of the Test Campaign and Test Matrix

The objective of the cylindrical test campaign – working title *Stepperino* – is to investigate the effect of BFS and FFS on the (local) regression rate. Table 1 lists the averaged data acquired during and after the respective tests. In the consecutive sections, the results will be examined in detail. Based on a previous numerical study of a different motor at ONERA [2], the step height is fixed to 10 mm (meaning a diameter difference of 20 mm). In order to facilitate the production of the fuel grains, only two fuel port diameters (50 mm and 70 mm) are considered. A total of 9 hot fire tests (T1-T9) have been conducted, out of which T5 exhibited anomalies during the start up and ignition phase. This is why T5 will not be considered for the following investigations.

The *Stepperino* campaign consists of four reference cases without steps, two with five seconds burn time and two with ten seconds burn time. Two BFS and FFS cases each are compared to these reference cases. In a stepped case, the diameter before and after the step is different (from 50 mm to 70 mm for BFS and vice-versa for FFS). Therefore, the stepped case needs to be compared to the no-step reference with the same diameter before the step and consequently with a different diameter after the step. This means the stepped cases are compared to two sub-references. For example, a BFS step case is compared to the 50 mm reference in the first half and to a 70 mm reference in the second half (after the step). This approach is depicted in Figure 5.

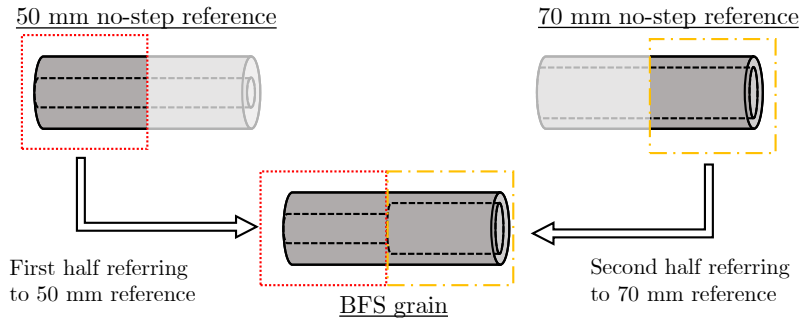


Figure 5: Visualization of two sub-references of BFS grain

Table 1: Overview of test conditions

Test	Config.	t_b [s]	\dot{m}_{ox} [kg/s]	O/F [-]	G_{avg} [kg/m ² s]	\bar{r} [mm/s]	m_f [g]
T1	70 mm ref.	10	0.391	24.54	93.5742	0.294	159.3
T2	50 mm ref.	10	0.443	20.38	180.585	0.589	217.4
T3	FFS (70/50 mm)	5	0.468	17.89	148.207	0.682	130.8
T4	BFS (50/70 mm)	3.972	0.465	20.5	153.987	0.5	90
T5	BFS (50/70 mm)	2.99	0.432	28.96	146.498	0.425	44.6
T6	BFS (50/70 mm)	5.117	0.517	18.75	161.115	0.77	141.2
T7	FFS (70/50 mm)	5.988	0.43	18.73	135.647	0.584	137.3
T8	70 mm ref.	5.07	0.504	25.1	125.67	0.285	102
T9	50 mm ref.	5.724	0.49	18.62	212.982	0.72	150.6

3.4 Experimental Results

The results of the *Stepperino* test campaign will be exploited in two ways. First, the local regression rate profiles along the fuel grain surface will be examined to find explanations for the mechanisms behind BFS and FFS regression rate enhancement. Subsequently, the space and time averaged regression rates will be compared and analyzed for all the cases to derive an indication into the effectiveness of BFS and FFS.

3.4.1 Surface Profiles

The surface profiles are obtained with the method explained in Section 3.2.1 and three exemplary scans are presented in Figure 6.

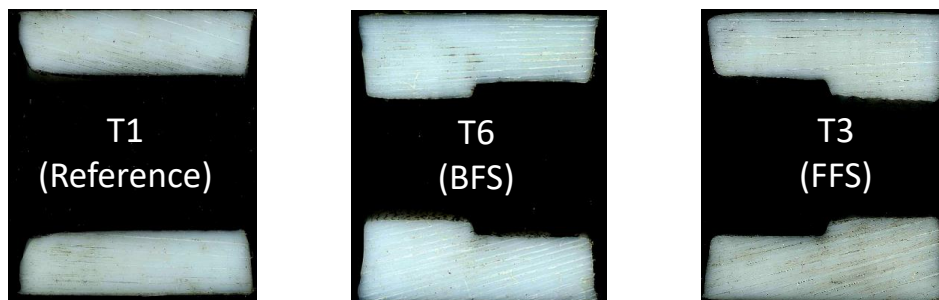


Figure 6: Exemplary scans of fuel grains after test

Figure 7 illustrates the initial diameter of Test 4 and Test 6. The position of the step is at zero axial position, and only the grain surface 40 mm before and after the step is considered in all following figures. This choice allows to exclude the lateral fuel surfaces and the injector effects at the beginning of the fuel grain which are not subject of investigation in this campaign. The diameter value displayed in the y-axis is the outer grain diameter (D) minus the inner diameter (d) to allow for a more convenient interpretation of the figure.

Looking at the final diameter of Test 4 and Test 6 in Figure 7, it becomes obvious that with increasing burn time the step becomes more and more rounded. Before the step, the regression seems to be almost parallel. On the other

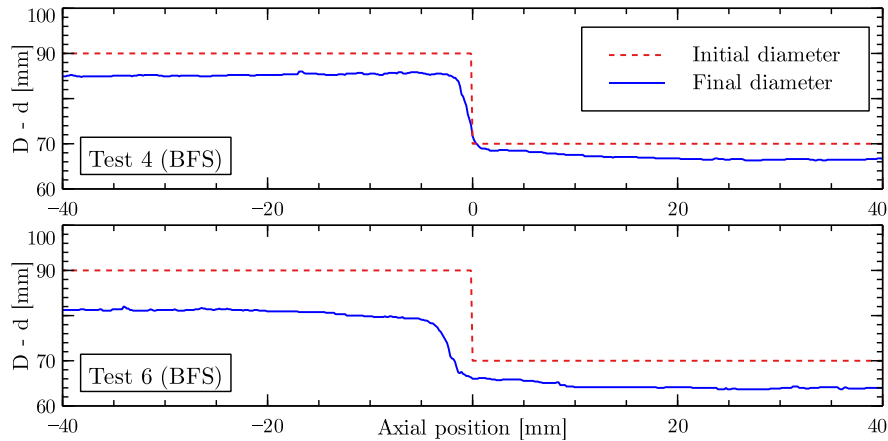


Figure 7: Initial vs. final diameter of BFS cases

hand, after the step, a small plateau is visible. This indicates that the local regression rate at this point is lower due to the flame being further away from the surface. After this plateau, however, the regression of the surface is elevated due to the increased mixing induced by the recirculation zone that forms itself behind the BFS. This effect has been already observed numerically during the parametric study [2] on a different motor at ONERA. This common trend becomes even more clear when looking at the regression rate profiles obtained using Equation 1. The results for the BFS are displayed in Figure 8. The red data-set is the BFS surface profile of Test 4 and Test 6 respectively. The blue and green data are the corresponding no-step reference cases at 5 and 10 second burn time. To recall, a reference case for BFS is composed of a 50 mm no-step grain in the first half, and a 70 mm no-step grain in the second half. This way, the regression rates of approximately the same G_{ox} are compared among each other. For Test 4, the regression rate before

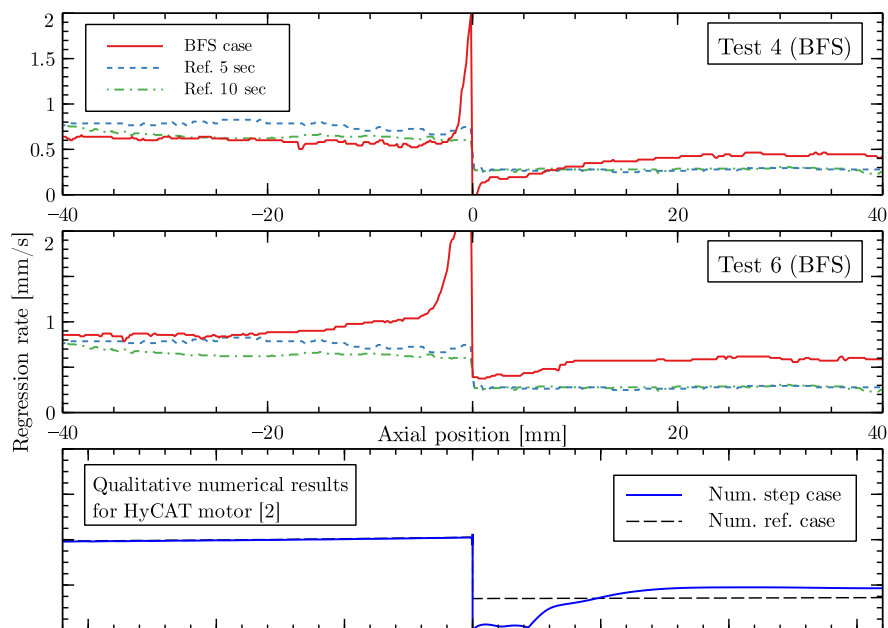


Figure 8: Regression rate profile of BFS cases

the step is almost identical to the reference cases. For Test 6, however, the regression rate increases already before the step. This is due to the progression of the step that has been visible in Figure 7: The step gets smoother and changes its shape, leading to a 'discontinuity' in the regression rate at the initial position of the step and a higher regression rate left from it. Directly after the step, the regression rate exhibits a minimum because of the flame being further away from the fuel surface. After a short distance, however, the regression rate increases over the reference cases due to the enhanced mixing and heat transfer of the recirculation zone.

Additionally, in the third part of Figure 8, the qualitative results of a numeric study [2] are shown. It is to be stressed that the results of the numerical study are only to be interpreted as qualitative comparison and are not intended as validation, as the simulations were done for the HyCAT motor at ONERA using H_2O_2 and HDPE and not for the *Stepperino* campaign. Nonetheless, these simulations allow us to relate the physical phenomena covered by the simulations qualitatively to the experimental cases. It becomes obvious that the effect of a regression rate minimum directly after the step is also visible for the numerical simulations. Interestingly, it seems that the decrease in regression rate after the step is slightly overestimated for the simulations. This could indicate that the turbulence model (Shear Stress Transport) or the combustion model are not perfectly suited to cover the effects of the BFS (for the detailed numerical set-up the reader is referred to [2]). This effect will be further discussed in the following section about the FFS regression rate profiles. Moreover, the large peak before the step is not captured by the simulations, as the simulations only represent the first instance in time, where the step is still vertical and has not changed its shape yet.

Turning to the FFS cases, Figure 9 shows the diameter profiles of the FFS fuel grains the same way as Figure 7 did for the BFS. Looking at Figure 9, the progression of the step from its initial state is clearly visible. Interestingly, shortly before the step, the profile is more regressed, forming a cavity. This hints at increased regression rate due to the positive effects of the recirculation zone that forms itself before the FFS. Moreover, directly after the FFS, another area of higher regression can be seen (clearly visible for Test 3 immediately after the step). This area of more regressed fuel indicates the length of the recirculation zone that forms after the FFS. Inside this recirculation zone mixing and turbulence are increased. Together with increased heat transfer to the fuel surface, these effects increase the regression rate locally. The positive effects of the recirculation zone induced by the steps become even more evident when

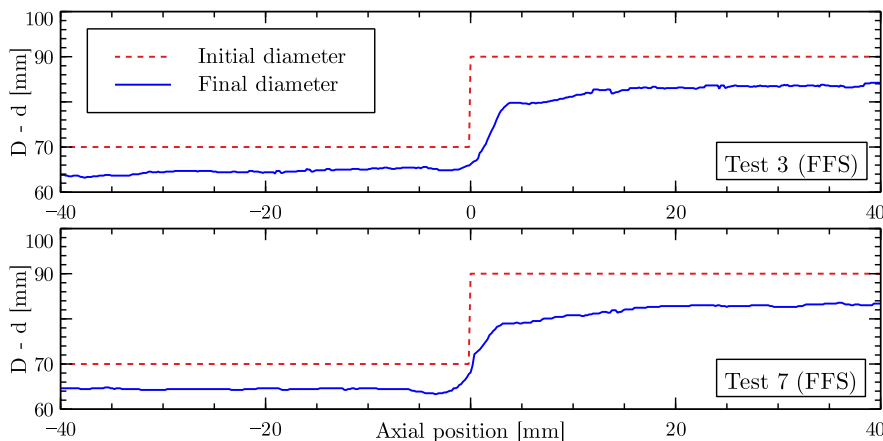


Figure 9: Initial vs. final diameter for FFS cases

considering the regression rate profiles of the FFS cases in Figure 10. Following the known approach, the regression rate of the FFS cases is plotted alongside the two respective reference cases. Here, the two distinct peaks of regression rate due to the recirculation zone become apparent. For the zone before the step, it is a small distinct peak (especially for Test 7), whereas for the zone behind the step it is rather an area of increased regression rate.

Compared to the reference cases, the profile before the step follows approximately the same qualitative shape, however, quantitatively the cases have higher regression rates. This fact is rather due to uncertainties in mass-flow rate than to the effect of the step, giving the fluctuations in oxidizer mass-flow during the different tests. After the FFS, however, the regression rate for the step cases is considerably higher directly after the step. Interestingly, the regression rate descends again to the level of the reference cases. This signifies that the effect of the recirculation zone for the FFS cases is limited in its length and diminishes with increasing distance to the step. This is contrary to what has been observed for the BFS cases (recalling Figure 8) where the effect of the recirculation zone increased the regression rate constantly over the reference cases for the remaining fuel grain length.

At the bottom of Figure 10, again, the corresponding numerical simulation on a FFS in a different motor is displayed. It is to be stressed that this should not serve to validate the simulation, it is to show how the same physical effects that could be observed in the experiments are covered by the simulations. Interestingly, the small peak in regression rate that is present in both FFS tests before the step cannot be seen in the numerical simulations. Likewise to the simulations for the BFS cases, in the simulations, the presence of a recirculation zone seems to decrease the regression rate locally and only increases the regression rate after the recirculation zones. This again indicates that the selected turbulence or combustion model of the simulation leaves room for improvements. This will be addressed in future work when conducting dedicated numerical simulations to match the experimental cases.

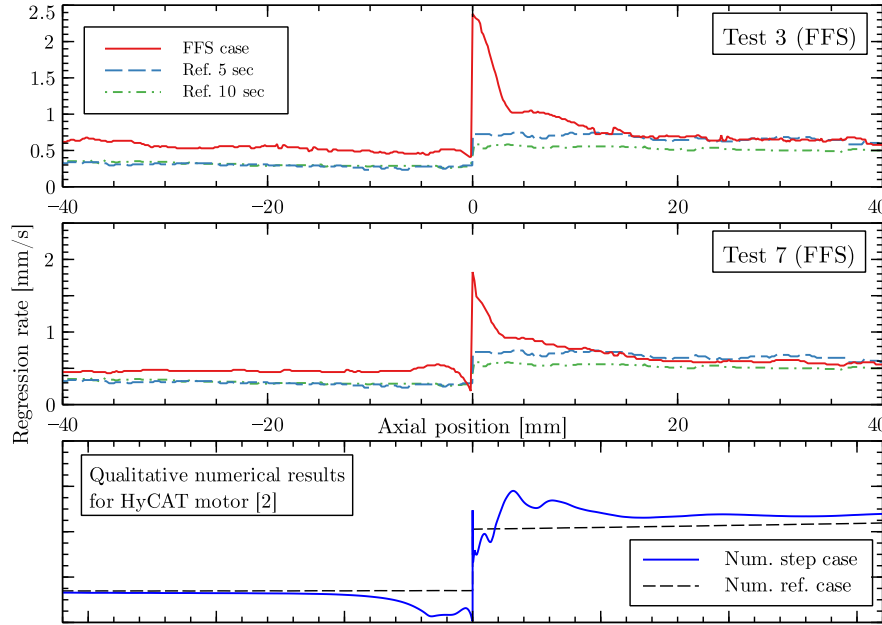


Figure 10: Regression rate profile of FFS cases

To conclude this section, the positive effect of BFS and FFS can be clearly followed in the regression rate profiles. The recirculation zone behind the BFS increases the regression rate after the step considerably compared to the reference cases. For the FFS cases, the increase of the regression rate is visible before and after the step, however, the peak in regression rate decreases with distance and descends to the level of the reference cases. Additionally, it has been shown that numerical simulations (carried out for a study that can be loosely related to our experiments) were able to predict qualitatively the shape of the regression rate profiles, with smaller differences which can be possibly traced back to the chosen turbulence closure and combustion model. This discrepancy will be addressed in the continuation of this work in the future.

3.4.2 Time and Space Averaged Method

In the previous section on surface profiles, the effect of the steps could be evaluated locally. Nonetheless, in order to understand the effect of FFS and BFS over the concerning grain length (40 mm before and after the step), we will concern ourselves with the space and time averaged regression rates. The space and time averaged regression rate \bar{r} can be calculated based on Equation 2. For the averaged mass flux the following expression is used:

$$G_{\text{ox,avg}} = \frac{4\dot{m}_{\text{ox}}}{\pi \cdot \left(\frac{D_0 + \bar{D}_f}{2}\right)^2} \quad (4)$$

with \bar{D}_f being calculated as:

$$\bar{D}_f = \frac{1}{x_1 - x_0} \int_{x_0}^{x_1} D_f(x) dx, \quad (5)$$

with x_0 and x_1 being -40 and 40 mm respectively (step being at $x = 0$ mm) as it was also the case in Figures 7 to 10. This way, we do not consider the injection effects and lateral grain surfaces. The space and time averaged regression rate is plotted in Figure 11. The red line represents the Marxman [12] fit in the form of $r = a \cdot G^n$; only for the reference cases. With the help of these data we can evaluate the effect of the steps on the whole fuel grain.

In total, the regression rate of the FFS cases lies above the reference trend (about 48 % for the case of T3). This is mainly due to the fact that the regression rate of these cases is already elevated for the first grain half, as an effect of the recirculation zone before the FFS. This was already visualized in Figure 10. For the BFS cases, T6 lies also above the reference trend (around 53 % increase) mainly due to the dominant increase in regression rate for the second half of the grain. T4 does not exhibit this increase, which we suspect to be related to the errors of the oxidizer mass flow estimation. There are two possible explanations for this. The first is that during the investigation of the experimental

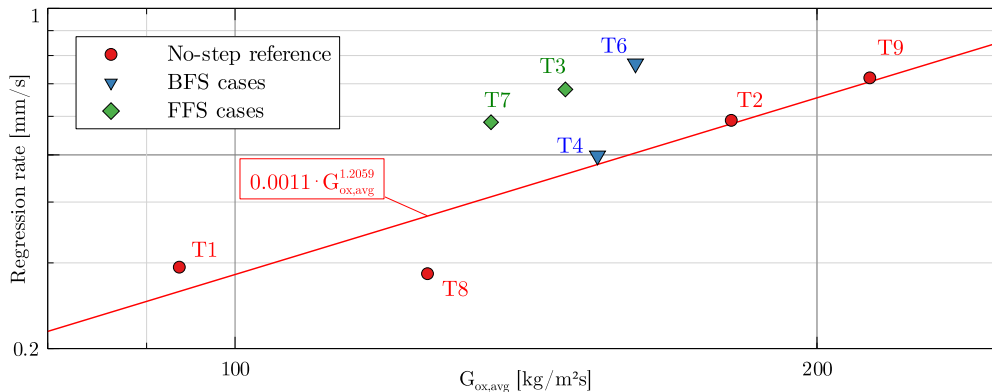


Figure 11: Averaged regression rate over whole fuel grain length

videos, we noticed a small leak in the pre-chamber for T4. Since we measure the total mass loss of the N_2O tank during the test, it is impossible to derive how much oxidizer really went through the fuel port. Moreover, T4 exhibited an unusual long ignition time during which some of the N_2O was vented through the unchoked nozzle. We suspect that these two effects in combination led to an overestimation of the oxidizer mass flow through the fuel port. Hence, the regression rate of T4 correlates to a higher virtual G_{ox} than what took place during the experiment. In reality, the data point should be shifted more to the left along the x-axis. Future studies with more data points will prove or disprove this hypothesis.

Having said this, the section of the space and time averaged regression rates can be concluded. It has been shown that both BFS and FFS have the potential to considerably increase the total regression rate. In this preliminary test campaign, most of the cases supported the assumption of increased regression rates due to BFS and FFS. A more extensive campaign will show whether this trend is maintained for a larger range of mass fluxes and initial conditions. One final remark on the exponent n for the Marxman fit needs to be made. The exponent is rather high for hybrid rocket motors. Typical values lie usually around 0.4-0.9 [13]. Nonetheless, Lengellé *et al.* [14] observed exponents for GOX/HDPE of 1.13 which lies around the same value as for the *Stepperino* campaign. We suspect that the high O/F ratios (around 20) in our campaign increase the dependency of the regression rate on the mass flux, visible in a higher exponent than 0.8, which would be the predicted value for diffusion limited HREs [13].

4. Stepped Geometries on Two-dimensional Slab Burner MOUETTE

In the previous sections we concentrated the investigation of stepped designs on cylindrical cases only. While these configurations are closest to a real use-case, the influence of the steps on the flow and most importantly the regression rate can only be assessed after the tests. That is why for the following sections we investigate the effect of a BFS and a FFS in the MOUETTE (*Moteur Optique pour ETudier et Tester Ergols hybrides*) slab burner with optical access at ULB.

4.1 MOUETTE Facilities

The ULB-ATM MOUETTE hybrid rocket slab burner, shown in Figure 12, has been developed to investigate the internal ballistics of hybrid rockets. The system operates with gaseous oxygen (GOX) as oxidizer and paraffin as fuel. The mass flow rate can be increased up to 100 g/s, with a maximum chamber pressure of 10 bar. The test bench is equipped with pressure transducers and K-type thermocouples in the feed system and in the chamber. The combustion behavior can be monitored with a high-speed camera, taking advantage of two optical accesses, which allows performing both chemiluminescence and for the future Schlieren techniques to acquire experimental data. The length of the fuel grain is 110 mm with a maximum height of 30 mm and 40 mm width. A detailed description of the burner features, design process and its capabilities is given in reference [15].

4.2 CH* Chemiluminescence of Stepped Geometries

The BFS and FFS paraffin slabs mounted in the combustion chamber before the test are displayed in Figure 13. The white arrows indicate the oxygen flow direction. The instantaneous flow-field over the stepped geometries taken from the high-speed camera can be seen in Figure 14. The CH* filter is used to detect the UV emissions of the CH radical

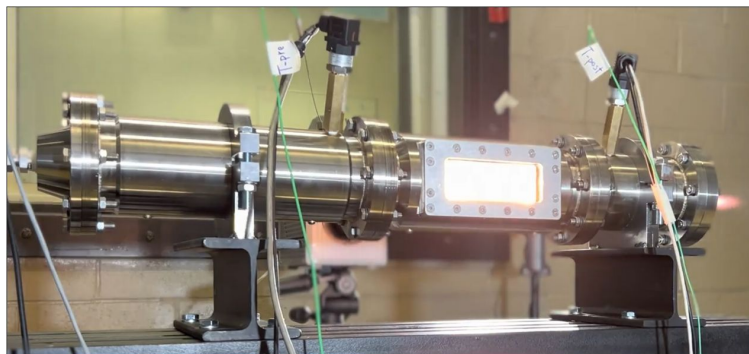


Figure 12: MOUETTE slab burner with optical access [15]. Printed with permission.

(430 nm) which can be directly interpreted as the chemical reaction zone. As a visual support, the silhouette of the respective step is suggested with white lines. An overview on the experimental data is given in Table 2.

Table 2: Overview of test conditions

Type	Step height [mm]	Burn time [s]	Chamber pressure [barg]	Mass flow [g/s]
BFS	10	5.46	2.48	79.2
FFS	10	7.24	3.33	95.85

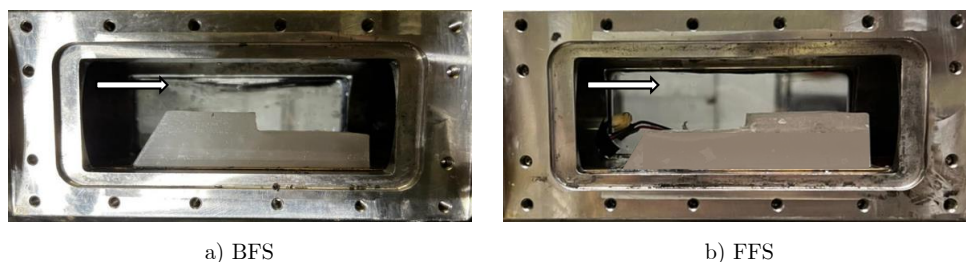


Figure 13: Paraffin slabs mounted in the combustion chamber

Although some flow characteristics can be already guessed from the high-speed images in Figure 14, due to the turbulent nature of the combustion, it is difficult to assess the details of the flow field. For this reason, we apply a method to average the turbulent nature of the combustion. Therefore, the full video is separated into frames (approximately 3000) and the frames are averaged using a moving average for each 100 frames. Using this process, the turbulent behavior of the combustion can be smoothed out and the images obtained remind remotely of Reynolds averaged simulations. In Figure 15, the moving average of the BFS case at the beginning and at the end of the burn is documented. As can be observed, the characteristics of the flow become more visible thanks to the moving average. At the beginning of the flow (upper part), the turbulent boundary layer is clearly visible and the first formation of a recirculation zone is noticeable. For the end of the burn (lower part) the recirculation zone is now fully developed and expands its influence over the whole fuel slab.

The same kind of averaged flow-fields are shown in Figure 16 for the FFS case. Likewise to Figure 15, the reaction zones become clearly visible due to the averaging process. In the upper part of Figure 16 at the beginning of the burn, the formation of the recirculation zone before and directly after the step can be recognized. Moving to the lower image (representing the end of the burn), both recirculation zones are fully developed, leading to a noisy picture, even after averaging. This hints at a high turbulence level.

While the running averaging method already allows us to better understand the flow-field, to fully resolve the flow-field characteristics over the stepped fuel slabs, another method is applied. The regression rate of HREs is directly dependent on the fuel surface temperature and therefore the heat transfer from the flame to the fuel surface. Therefore, higher turbulence levels and recirculation zones locally increase regression rates. Enhanced regression rates lead to augmented combustion and therefore higher CH^* intensity. Hence, the intensity of each frame can be used to derive

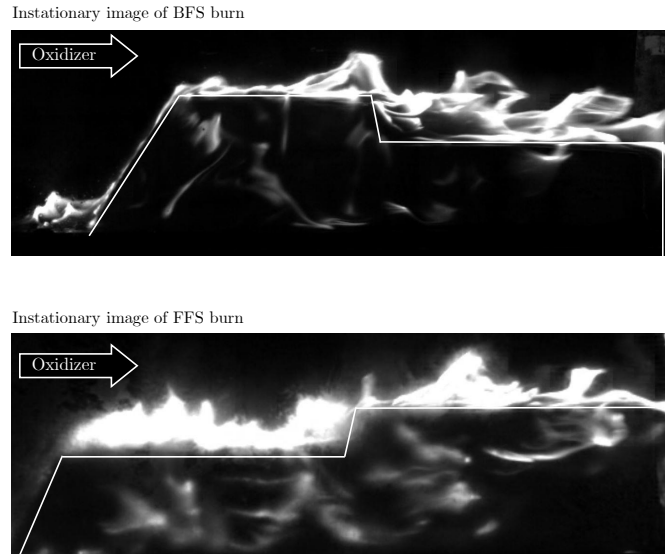


Figure 14: Instantaneous CH* images of BFS and FFS

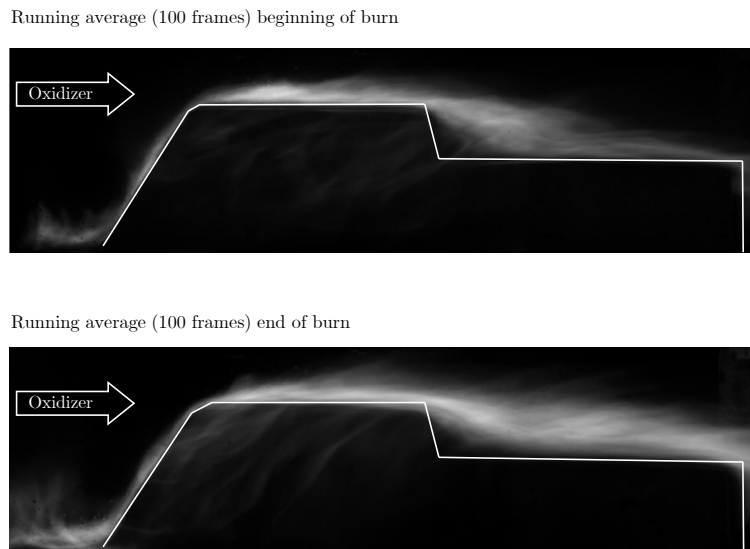


Figure 15: Moving average of BFS case

zones of higher regression rates and combustion activity. For this reason, instead of averaging each frame, we total the gray value (representing the CH* intensity) of each pixel in each frame during the burn time along the y-axis. This allows to detect zones of higher chemical reaction. With this information we can connect the zones of higher intensity directly to areas with higher turbulence and regression rates. The process is described with Equation 6:

$$I(x) = \frac{1}{y_{\max}} \sum_{y=0}^{y_{\max}} \sum_{t=t_{\text{ign}}}^{t_{\text{burn}}} \frac{I(x, y, t)}{t_{\text{burn}}}, \quad (6)$$

with I being the Intensity or gray value, y_{\max} the maximum frame height and t_{burn} and t_{ign} the burn and ignition time, respectively. Using Equation 6, an intensity profile along the x-axis can be calculated which is presented in Figure 17 for the BFS case. Additionally, the summarized intensity of the image is represented on the upper half of the image, allowing to relate the flow phenomena directly to the derived intensity curve of Equation 6. As anticipated, the peaks of the intensity profile correlate exactly to the areas of recirculation and increased turbulence and, thus, higher regression rates. The first peak of the intensity curve is explained recalling Figure 13. The way the grain holder of MOUETTE is designed, each fuel slab consists of a rather dominant step at the beginning of the grain (for a detailed reasoning into

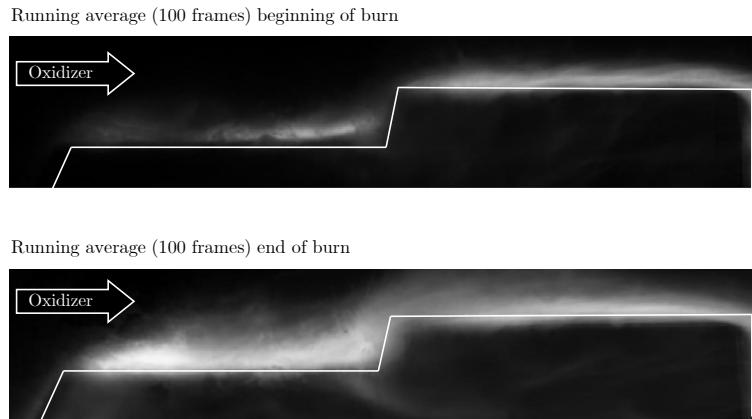


Figure 16: Moving average of FFS case

the design choices of the grain holder and MOUETTE in general, the reader is referred to [15]). Since this BFS at the beginning of the fuel grain induces a recirculation zone – similar to the step in the middle of the fuel grain – a distinct peak is noticeable at the beginning of the fuel grain. The second peak of the intensity can be found not far downstream from the main step in the middle. This correlates closely to what we observed for the cylindrical BFS cases in Figure 8 and supports the theory that the intensity can be used as a qualitative indicator for increased regression rates: The BFS in the middle of the fuel grain induces a recirculation zone length which locally increases the regression as a result.

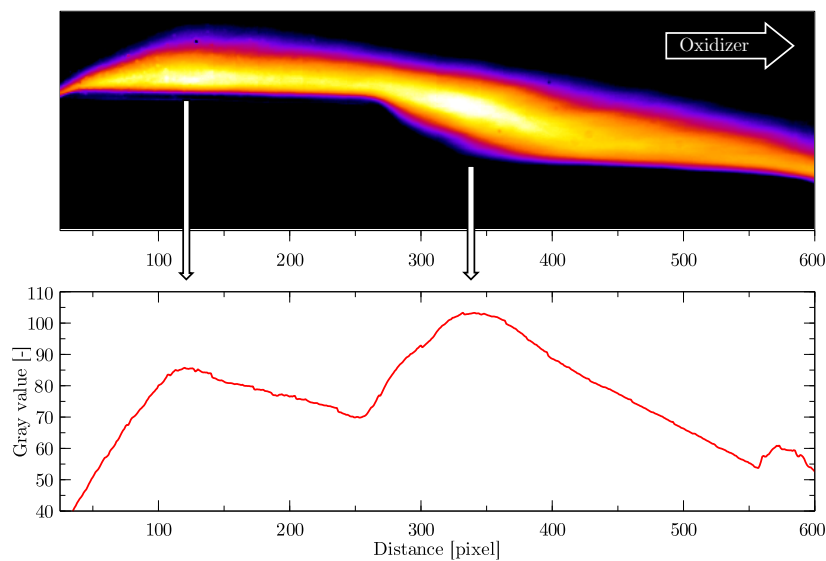


Figure 17: Intensity profile of BFS case

The same intensity approach is followed for the FFS case and is depicted in Figure 18. Again, the observations of the intensity plot are perfectly in line with the behaviour of the cylindrical fuel grains in Figure 10. Three peaks in intensity are distinguishable. The first peak is due to the same phenomena that was explained for the BFS MOUETTE case. The beginning of the fuel slab consists of a step, therefore triggering a recirculation zone. The second peak lies directly before the FFS. Recalling Figure 10 of the cylindrical FFS study, the behaviour of the slab burner and the cylindrical case are identical. The regression rate immediately before the FFS is augmented. The third, less pronounced peak can be derived from the recirculation zone directly after the FFS. Likewise to the cylindrical cases the regression rate shortly after the FFS is elevated.

Concluding this Section, we have obtained the same physical phenomena as the experimental results of Section 3.4.1, only using image processing. Moreover, we have shown that the effect of steps can be reproduced also for 2D geometries and using paraffin instead of HDPE. This justifies the use of slab burners with visual access to further investigate the effect of stepped geometries on the regression rate in the future. One possible adjustment to the experimental set-up would be to use longer fuel grains to eliminate the effect of the first step at the beginning of the fuel grain.

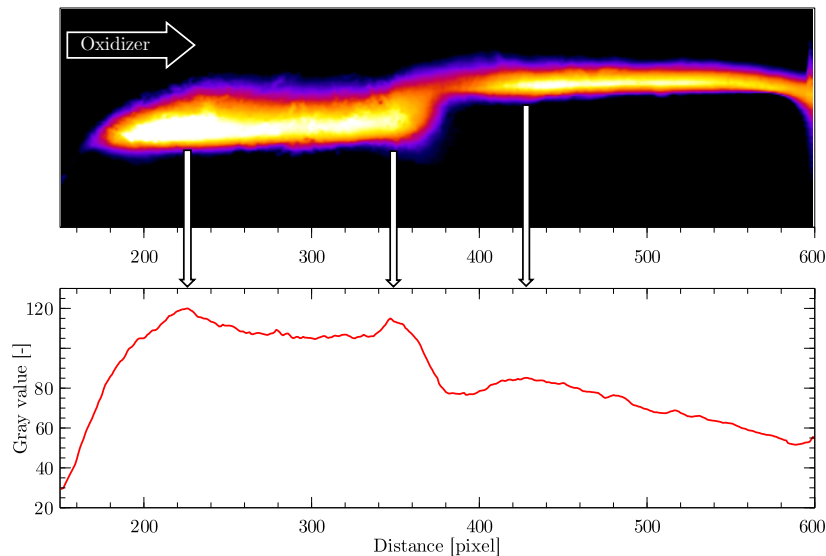


Figure 18: Intensity profile of FFS case

5. Concluding Remarks

In this work, the theoretical positive effects of BFS and FFS inside HREs could be shown experimentally. For the cylindrical motor, the FFS increased the average regression rate 48 % above the reference trend line, in the case of BFS the increase was even 53 %. Thanks to detailed investigations of the regression rate profiles along the fuel grain's surface, the areas of locally increased regression rates could be qualitatively assessed. With the help of these regression rate profiles, at this point, we can derive the following considerations for the over-arching goal to distribute multiple BFS and FFS along a profile:

1. For BFS, the locally increased regression rate is mostly confined to downstream the step position. After the step, the regression rate is increased by a considerable amount over the reference. Based on these profiles, we anticipate that a potential second BFS (or FFS for that matter) should be placed at around 30 mm downstream the BFS which correlates to 3 times the step height. Up to this length-to-height ratio of 3, the local regression rate continues to increase, until it slowly starts descending (refer also to Figure 8).
2. For the FFS cases, the regression rate enhancement is already noticeable at 5 mm before the step, corresponding to a length-to-height ratio of 0.5. After the step, increased regression rate profiles are measurable until approximately 20 mm after the step yielding a length-to-height ratio of 2. Combining these two areas of increased regression rates, the total length-to-height ratio denotes to 2.5 (recalling Figure 10). Translating this to potential multiple steps, it is postulated that distributing FFS spaced 2.5 their step height should increase the regression rate the most.

As for the 2D-slab burner campaign, it has been shown that the effects of steps are also existing for paraffin fuels and in the two-dimensional domain. Using image post-processing through the optical access of the slab burner, the areas of higher regression rates could be already identified during the burn through an analysis of the CH^* intensity. These areas of the 2D campaign correspond precisely to the cylindrical test campaign that uses HDPE. This allows us in the future to investigate the instantaneous regression of the steps with time more conveniently through an optically accessible slab burner like MOUETTE.

Another field of interest is the influence of BFS and FFS on pressure oscillations and combustion efficiency. With the help of a piezoelectric pressure transducer, the impact of the steps on the chamber pressure will be assessed in the future. We expect, based on the study of Lee *et al.* [7], that pressure oscillation are less a concern for the BFS cases and more for the FFS cases. FFS resemble diaphragms in the fuel port that usually trigger pressure oscillations in HREs.

Concluding this work, the feasibility of BFS and FFS and their potential to increase the regression rate in HREs have been preliminary proven. For the future, the interaction of multiple steps needs to be evaluated, especially the interaction of a FFS and BFS is of high interest as well as building a larger experimental data base. With these data, finally, a fully stepped fuel port profile can be designed and evaluated numerically and experimentally.

Acknowledgments

The authors would like to thank the technical experts at ULB-ATM for their support before and after the experimental test campaigns, and Laurent Ippoliti at ULB for his expertise in data acquisition. The seamless development of the *communicating vessel* method was primarily driven by Giulio Pelenghi, intern at DMPE/LPF at ONERA. Moreover, we would like to acknowledge the invaluable support of Quentin Levard at ONERA in terms of image post-processing. Finally, we are thankful for the Belgian Air Force in Beauvechain for hosting our test campaign(s).

The project leading to this application has received funding from the European Union's Horizon 2020 research and innovation programme under the Marie Skłodowska-Curie grant agreement No 860956. It is part of the ASCenSIon project, an Innovative Training Network (ITN) to advance space access capabilities (<https://ascension-itn.eu/>).

References

- [1] A. Okninski, W. Kopacz, D. Kaniewski, and K. Sobczak, "Hybrid rocket propulsion technology for space transportation revisited - propellant solutions and challenges," *FirePhysChem*, Dec. 2021.
- [2] C. Glaser, J. Hijlkema, and J. Anthoine, "Approximating Idealized Hybrid Rocket Fuel Port Geometries Using Steps," in *8th Edition of the Space Propulsion Conference, Portugal*, May 2022.
- [3] C. Glaser, J. Hijlkema, and J. Anthoine, "Evaluation of Regression Rate Enhancing Concepts and Techniques for Hybrid Rocket Engines," *Aerotecnica Missili & Spazio*, May 2022.
- [4] A. Gany and Y. Timnat, "Parametric study of a hybrid rocket motor," *Israel Journal of Technology*, vol. 10, pp. 85–96, Jan. 1972.
- [5] M. Grosse, "Effect of a diaphragm on performance and fuel regression of a laboratory scale hybrid rocket motor using nitrous oxide and paraffin," in *45th AIAA/ASME/SAE/ASEE Joint Propulsion Conference and Exhibit*, (Reston, Virginia), American Institute of Aeronautics and Astronautics, Aug. 2009.
- [6] M. Dinesh and R. Kumar, "Utility of Multiprotrusion as the Performance Enhancer in Hybrid Rocket Motor," *Journal of Propulsion and Power*, vol. 35, pp. 1005–1017, July 2019.
- [7] J. Lee, S. Rhee, J. Kim, and H. Moon, "Combustion Instability Mechanism in Hybrid Rocket Motors with Diaphragm," *Journal of Propulsion and Power*, pp. 1–10, Oct. 2021.
- [8] H. Sakashi, Y. Saburo, H. Kousuke, and S. Takashi, "Effectiveness of Concave-convex Surface Grain for Hybrid Rocket Combustion," *48th AIAA/ASME/SAE/ASEE Joint Propulsion Conference and Exhibit*, July 2012.
- [9] M. Kumar and P. Joshi, "Regression rate study of cylindrical stepped fuel grain of hybrid rocket," *Materials Today: Proceedings*, vol. 4, no. 8, pp. 8208–8218, 2017.
- [10] M. Bouziane, A. E. De Morais Bertoldi, P. Milova, P. Hendrick, and M. Lefebvre, "Development and Testing of a Lab-scale Test-bench for Hybrid Rocket Engines," in *SpaceOps Conferences*, American Institute of Aeronautics and Astronautics, May 2018.
- [11] J. Schindelin, I. Arganda-Carreras, E. Frise, V. Kaynig, M. Longair, T. Pietzsch, S. Preibisch, C. Rueden, S. Saalfeld, B. Schmid, J.-Y. Tinevez, D. J. White, V. Hartenstein, K. Eliceiri, P. Tomancak, and A. Cardona, "Fiji: an open-source platform for biological-image analysis," *Nature Methods*, vol. 9, pp. 676–682, July 2012.
- [12] G. Marxman and M. Gilbert, "Turbulent boundary layer combustion in the hybrid rocket," *Symposium (International) on Combustion*, vol. 9, pp. 371–383, Jan. 1963.
- [13] C. Carmicino and A. R. Sorge, "Role of injection in hybrid rockets regression rate behaviour," *Journal of Propulsion and Power*, vol. 21, pp. 606–612, Jul 2005.
- [14] G. Lengelle, B. Fourest, J. Godon, and C. Guin, "Condensed-phase behavior and ablation rate of fuels for hybrid propulsion," in *29th Joint Propulsion Conference and Exhibit*, American Institute of Aeronautics and Astronautics, Jun 1993.
- [15] R. Gelain, F. Angeloni, A. E. De Morais Bertoldi, and P. Hendrick, "Design and commissioning of the MOUETTE hybrid rocket slab burner," in *9th European Conference for Aeronautics and Space Sciences (EUCASS)*, 2022.